JOURNAL OF SPACECRAFT AND ROCKETS
Vol. 43, No. 1, January–February 2006

Multipoint Nose Shape Optimization of Space Launcher Using Response Surface Method

Jae-Woo Lee,* Byung-Young Min,† and Yung-Hwan Byun‡
Konkuk University, Seoul 143-701, Republic of Korea
and
Sang-Jin Kim§
Agency for Defense Development, Daejeon 305-605, Republic of Korea

A multipoint optimization technique has been implemented to improve the performance over a wide operating range for the shape design of a nose fairing to a space launcher. The response surface method is implemented to reduce the computational effort during optimization. For the optimization model, the drag represents the objective function, and the design constraints are based on the maximum allowable surface heat transfer and the minimum internal volume for the nose fairing. The data for the response surfaces are obtained by solving the Navier–Stokes equations. The key flight events are simplified for efficient multipoint design, and separate response surfaces have been constructed for each design point. The response surfaces are combined together with a weighting factor to construct an objective function. Optimization through separate response surface and weighting functions shows good effectiveness for the two test cases: drag minimization and combination of drag/heat-transfer minimization. Finally, with the validated optimization approach, the space launcher nose shape, which undergoes the least drag during the whole flight mission while satisfying given heat-transfer constraint, is designed. The shape function approach and the nonuniform rational B-spline curve approach are implemented and compared for modeling the nose geometry. The optimization approach proposed in this study results in a nose fairing shape of the launcher that has a 24% improved drag characteristic when compared to the baseline shape.

Nomenclature

a = speed of sound
C_D = drag coefficient
C_h = Stanton number
C_p = pressure coefficient
$C(u)$ = nonuniform rational B-spline (NURBS) curve
D = drag
e_0 = total energy per unit mass
F, G = spatial flux
F_v, G_v = viscous flux
$F(\boldsymbol{X})$ = objective function
$g(\boldsymbol{X})$ = constraint function
H = axisymmetric source term
H_v = axisymmetric viscous source term
h_{aw} = adiabatic wall enthalpy
h_w = wall enthalpy
J = Jacobian from the coordinate transformation
l = nose length of the launcher
M = Mach number
$N_{i,k}(u)$ = B-spline blending function
P = static pressure
$\boldsymbol{P}_i$ = coordinate vector of the ith control point
$\boldsymbol{Q}$ = conservative variable vector
q = dynamic pressure
$\dot{q}_w$ = surface heat flux
q_x, q_y = heat flux in x and y directions
R_a = Reynolds number based on the sonic velocity
R^2_{adj} = coefficient of determination
r = radius
t = time, or knot value
U, V = contravariant velocity
$\boldsymbol{u}$ = velocity vector component in x direction, or NURBS curve parameter
V = internal volume
$\boldsymbol{v}$ = velocity vector component in y direction
w_i = weighting factor for control point of NURBS curve
X = design matrix
x, y = Cartesian coordinates
x_i = design variable
y_i = shape function
δ = entropy fixing value
δ^* = user-defined small value
λ = eigenvalue
ξ, η = transformed coordinates in the computational domain
$\xi_x, \xi_y, \eta_x, \eta_y$ = metric from the coordinate transformation
ρ = density
τ = shear stress
ω = weighting factor

Introduction

CURRENT research in launch-vehicle development is directed at low-Earth-orbit satellite launchers, cost-saving launchers such as evolved expendable launch vehicles, single- and two-stage-to-orbit reusable launch vehicles, and air-launching vehicles for small or microsatellites.[1]

Important factors to be considered in the aerothermodynamic design of satellite-launching vehicles are aerodynamic drag, surface

---

Presented as Paper 2002-0106 at the AIAA 40th Aerospace Sciences Meeting, Reno, NV, 14–17 January 2002; received 31 May 2004; revision received 27 May 2005; accepted for publication 31 May 2005.

*Associate Professor and Director, Center for Advanced e-System Integration Technology, Department of Aerospace Engineering, 1 Hwayang, Gwangjin; jwlee@konkuk.ac.kr. Member AIAA.

†Graduate Research Assistant, Department of Aerospace Engineering, 1 Hwayang, Gwangjin. Member AIAA.

‡Professor, Center for Advanced e-System Integration Technology, Department of Aerospace Engineering, 1 Hwayang, Gwangjin. Senior Member AIAA.

§Researcher, Aircraft/Missile Development Center. Member AIAA.

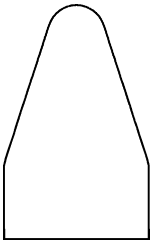

Fig. 1 Nose shape of the KSR-III.

heat transfer, and internal volume for payload accommodation. Although early research efforts have centered around analytical or experimental approaches, advances in computational methods have enabled the use of numerical optimization to be the dominant method in aerodynamic design.

Single-point design optimization results can guarantee the best performance at that design condition but show deteriorating performance for the off-design conditions. This can be overcome by employing a multipoint design optimization procedure for the entire flight mission envelope.

Multipoint design optimization has been implemented to improve the performance at off-design conditions in the design of the transonic airfoils.[2,3] By introducing weighting factors, multipoint drag minimization with a target pressure optimization technique[3] for the inverse design was performed. However, the impact of the large computational load required for the multipoint design also needs to be considered.

A system sensitivity analysis can be performed using rigorous and iterative analysis calculations. However, it is not conducive to use whole design space in the optimization because of the demand for computational resources by realistic applications. Numerical noise generated in the implementation of numerical analysis codes with the use of gradient-based optimization algorithms can lead to erroneous local optimal solutions.[4]

However, this large computational load in multipoint design optimization can be effectively reduced by using the response surface method (RSM). When used with computational fluid dynamics (CFD) analysis, RSM greatly reduces computational time by replacing complex analysis computer code with simple polynomials of design variables. Therefore, an optimization technique, which requires large number of functional evaluations such as genetic algorithm, can be implemented even on a personal computer. RSM has been implemented successfully in the single-point space launch vehicle design.[5]

RSM is a statistical method that can be used to approximate the objective function and constraint functions with a limited number of analysis calculations by using "the design of experiments theory."[6] RSM is ideal for multidisciplinary design and optimization problems.[7]

In this study, the optimum nose fairing shape of space launchers will be designed by employing RSM. Several operational conditions will be considered. Drag, surface heat flux, and total drag force experienced during the entire flight are considered separately or combined as design objectives. The design constraints consist of surface heat flux, internal volume, and fineness ratio of the nose fairing.

For realistic analysis and design, the full Navier–Stokes equations are employed for the design optimization. Available operational conditions and experimental or computational results of the rocket under development are used for this multipoint design optimization study. As a result of this study, the optimum shape for the nose fairing can be applied to the Korean three-staged rocket KSR-III. The baseline of this study is the nose of KSR-III as shown in Fig. 1.

Aerodynamic Analysis Method

The two-dimensional/axisymmetric Navier–Stokes equations for unsteady, compressible flow are selected as the governing equations [Eq. (1)] The spatial flux vectors $\boldsymbol{F}$, $\boldsymbol{G}$, and the viscous terms $\boldsymbol{F}_v$ and $\boldsymbol{G}_v$ are given by Eq. (2), using contravariant velocities U and V.

$$\frac{\partial \boldsymbol{Q}}{\partial \boldsymbol{t}} + \frac{\partial \boldsymbol{F}}{\partial \xi} + \frac{\partial \boldsymbol{G}}{\partial \eta} + \alpha H = \frac{\partial \boldsymbol{F}_v}{\partial \xi} + \frac{\partial \boldsymbol{G}_v}{\partial \eta} + \alpha H_v \tag{1}$$

$$\boldsymbol{Q} = \frac{1}{J}\begin{bmatrix} \rho \\ \rho u \\ \rho v \\ \rho e_0 \end{bmatrix}, \qquad \boldsymbol{F} = \frac{1}{J}\begin{bmatrix} \rho U \\ \rho u U + \xi_x p \\ \rho v U + \xi_y p \\ (\rho e_0 + p)U \end{bmatrix}$$

$$\boldsymbol{G} = \frac{1}{J}\begin{bmatrix} \rho V \\ \rho u V + \eta_x P \\ \rho v V + \eta_y p \\ (\rho e_0 + p)V \end{bmatrix}$$

$$\boldsymbol{F}_v = \frac{1}{J R_a}\begin{bmatrix} 0 \\ \xi_x \tau_{xx} + \xi_y \tau_{xy} \\ \xi_x \tau_{xy} + \xi_y \tau_{yy} \\ \xi_x \beta_x + \xi_y \beta_y \end{bmatrix}, \qquad \boldsymbol{G}_v = \frac{1}{J R_a}\begin{bmatrix} 0 \\ \eta_x \tau_{xx} + \eta_y \tau_{xy} \\ \eta_x \tau_{xy} + \eta_y \tau_{yy} \\ \eta_x \beta_x + \eta_y \beta_y \end{bmatrix}$$

$$H = \frac{1}{yJ}\begin{bmatrix} \rho v \\ \rho u v \\ \rho v^2 \\ (\rho e_0 + p)v \end{bmatrix}, \qquad H_v = \frac{1}{yJR_a}\begin{bmatrix} 0 \\ \tau_{xy} \\ \tau_{uu} - \tau_{\theta\theta} \\ \beta_y \end{bmatrix} \tag{2}$$

$$\beta_x = \boldsymbol{u}\tau_{xx} + \boldsymbol{v}\tau_{xy} - q_x, \qquad \beta_y = \boldsymbol{u}\tau_{xy} + \boldsymbol{v}\tau y_{yy} - q_y \tag{3}$$

For the two-dimensional flow, α is zero and is equal to 1 for the axisymmetric flow.

Roe's flux-difference-splitting scheme is implemented for the inviscid spatial discretization with the monotonic upstream-centered scheme for conservation laws.[8] Entropy fixing is needed to avoid numerical oscillations when applying Roe's scheme to a blunt body, such as the launcher nose shape. Harten–Yee type[9,10] entropy fix is employed in this study, given by the following function:

$$|\lambda| = [(\lambda^2 + \delta^2)/2\delta] \qquad \text{if} \qquad |\lambda| < \delta \tag{4}$$

where

$$\delta = \delta^*[|U| + |V| + (a/2)(\nabla\xi + \nabla\eta)]$$

In this equation, λ is the eigenvalue, a is the sonic velocity, and δ^* is the user-defined small value. A universal value of δ^*, which avoids numerical oscillations, is used for all cases because any variation in δ^* will affect the surface heat transfer. The minmod limiter[8] is used to remove solution oscillations from capturing strong shock waves. Fully implicit lower-upper symmetric Gauss–Seidel algorithm scheme[11] is implemented for time integration.

For improved computational efficiency, a coarse-grid system is selected that guarantees solution accuracy. This is achieved by investigating the convergence rate and the converged solutions of several grid systems with the baseline configuration given by the freestream conditions of Mach number 4.6 and Reynolds number 1.42×10^7. This freestream condition corresponds to an atmospheric condition of 31-km altitude, which is one of the design points used. From the result of Fig. 2, the 100×85 grid system has been selected with

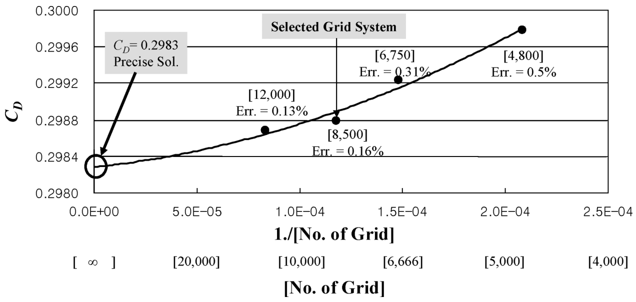

Fig. 2 Result of grid density test.

moderate stretching near the fairing surface. To maintain consistency in the Stanton-number calculation, the grid space just above the surface at the stagnation point is kept the same for all cases.

Validation of the Numerical Approach

10-deg Wedge and Cone

To validate the CFD analysis code for inviscid flow, a 10-deg wedge and cone shapes are numerically analyzed for the freestream Mach number of 6.0 (Ref. 12). The computational grids used are 101×31. Figure 3 shows the isodensity contours of the wedge and cone shapes. The results including the shock angles show good agreements with the exact solutions of NACA R1135 (Ref. 13) for both wedge and cone shapes.

Flow Around the Compression Corner

Flow phenomena of the compression corner are numerically investigated and compared with the experimental results of Holden and Moselle[14] to check the accuracy of the analysis code for the boundary-layer flow including separation. Figure 4 shows the separated flow around a compression corner with relatively big wedge angle. Down from the reattachment point the boundary-layer thickness becomes thin. The friction and the heat-transfer rate across the wedge surface become large. Moreover, the compression waves generated at the corner hit the leading-edge shock waves; hence, the resulting expansion wave and the shear layer affect the flow pattern of the ramp surface. The experiment was performed at the Calspan 48-in. shock tunnel, and the model consists of a flat plate and 24-deg wedge.

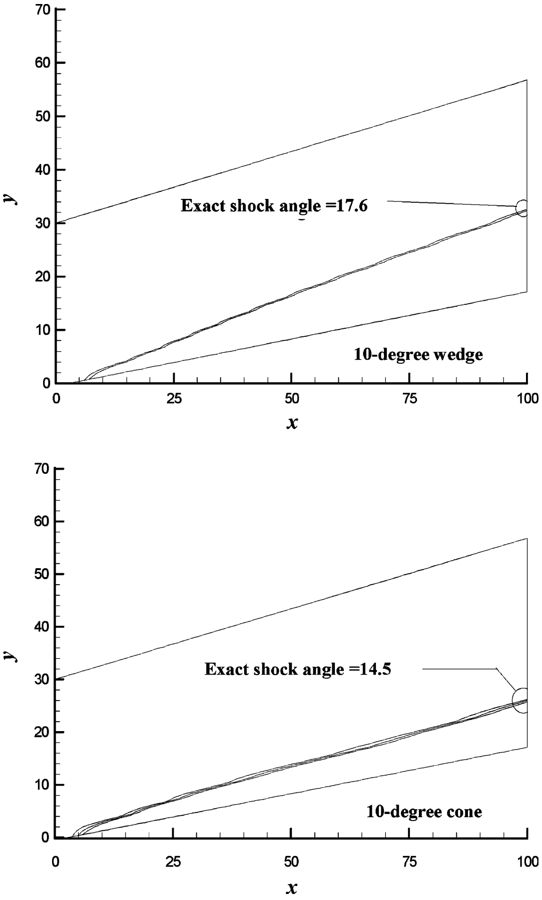

Fig. 3 Density contour of 10-deg wedge and cone.

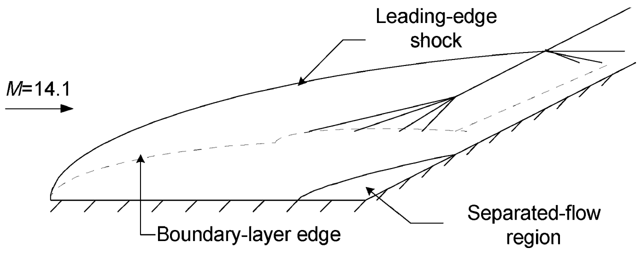

Fig. 4 Compression corner.

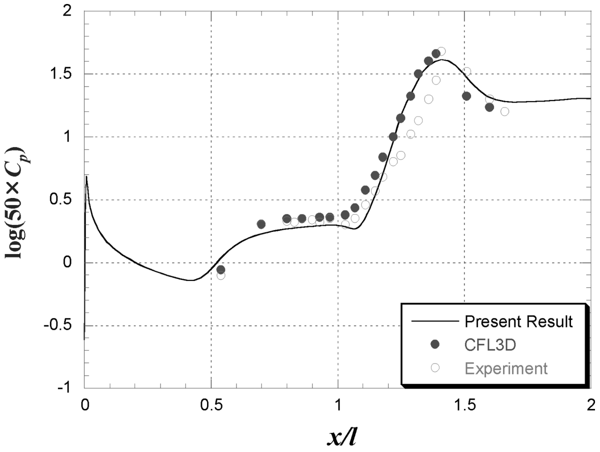

Fig. 5 Comparison of the surface pressure around the compression corner[17] (wedge angle 24 deg and freestream Mach number 14.1).

The freestream flow conditions are as follows: Mach number of 14.1, temperature of 160°R, Reynolds number of 7.2×10^4 (1/ft), and surface temperature of 535°R. Because the Reynolds number is small, the flow can be treated as a laminar, and no turbulent effects are considered. Rudy et al.[15] validated four Navier–Stokes computer codes using the experimental results of Holden and Moselle. Lee and Lewis[16] investigated the accuracy of the test time estimation.

For the numerical simulation for this problem, the 141×61 grid system was used. Figure 5 (Ref. 17) shows the surface-pressure coefficients compared with the experiments and CFL3D result.[17] Good agreement was obtained around the separation region and slightly higher value at the wedge surface than the experimental result. The general tendency is very similar to the CFL3D result.

Body Geometry Representation Techniques

Two body configuration generation techniques are implemented: a shape function approach and nonuniform rational B-spline (NURBS) curve approach.

According to Vanderplaats and Hicks,[18] existing airfoils are a good selection for shape functions. The coefficients of the shape functions are the design variables for the optimal design of the airfoils. When initial geometry information about the body to be designed is available, it is proven to be an efficient approach because the number of design variables can be greatly reduced.

NURBS is an alternate approach to generating a body configuration during optimization because it has greater capability when compared to the shape function method. In the launcher nose shape optimization problem, the coordinates of the control points are selected as design variables.

In this study, both approaches are compared for their configuration generation capability and the optimization result for the same nose fairing design problem.

Combination of Shape Functions

For the drag minimization of the space launch vehicle with a specified maximum heat flux and minimum internal volume constraints, the following simple body shapes are selected as shape functions: 1) minimum drag shapes like the von Kármán ogive; 2) the power-law body with power index n of 0.69; 3) blunt shapes, which have small surface heat-transfer rate, like the paraboloid; and 4) the sphere-cone.[19]

To alleviate the heat flux at the nose tip, the sharp nose tips of the von Kármán ogive and power-law body are replaced with a sphere. The fineness ratio (length/base diameter) is kept the same. The shape functions and the baseline configuration are shown in Fig. 6.

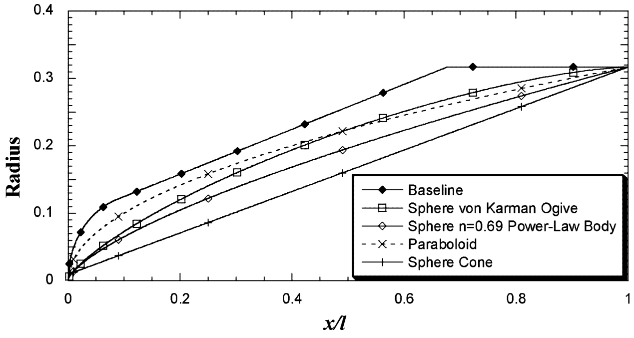

Fig. 6 Baseline shape and shape functions.

The configuration is expressed as a combination of the shape functions. To maintain the base diameter, a cone shape y_5 is added as shown in Eq. (5):

$$y = \sum_{i=1}^{4} x_i y_i + (1 - x_1 - x_2 - x_3 - x_4) y_5 \tag{5}$$

where y_1 is the sphere/von Kármán ogive, y_2 is the sphere/$n = 0.69$ power-law body, y_3 is the paraboloid, y_4 is the sphere-cone, y_5 is the cone, and x_i is the weighting factor of each shape function (the design variable).

Representation of the Configuration Using NURBS Curves

NURBS Curve

Among the analytical representations of body geometries, the Bezier and the NURBS curves are the most common. To represent complex geometries using the Bezier curve, many control points are required, which results in increasing the order of the polynomial and fluctuation of the curve generated. Modification of any control point on the curve results in unexpected variation of other points because each point along the entire curve is interlinked.

To generate complex curves, a B-spline blending function can be used to replace the Bernstein polynomials $B_{i,n}(u)$ employed in a Bezier curve. B-spline blending function can specify the order of the polynomial irrespective of the number of control points. By limiting the range of the parameter u, it is possible that only a small number of control points will affect the curve shape that is generated.

Order k NURBS curve, which employs the B-spline blending function, is as follows[20]:

$$C(u) = \frac{\sum_{i=0}^{n} N_{i,k}(u) w_i \boldsymbol{P}_i}{\sum_{i=0}^{n} N_{i,k}(u) w_i}, \qquad 0 \le \boldsymbol{u} \le n - k + 2 \tag{6}$$

where $\boldsymbol{P}_i$ is the coordinate vector of the ith control point and $n + 1$ is the number of control points. The weighting factor w_i determines the amount of influence of each control point on the curve shape generated. NURBS can generate various curves when describing the body geometries with only a few number of control points, using the allowable four degrees of freedom (DOF) given by the three DOF of the B-spline curve and one weighting factor.[21]

$N_{i,k}(u)$ represents order k B-spline blending function and is given by Eq. (7):

$$N_{i,k}(u) = \frac{(\boldsymbol{u} - t_i) N_{i,k-1}(u)}{t_{i+k-1} - t_i} + \frac{(t_{i+k} - \boldsymbol{u}) N_{i+1,k-1}(u)}{t_{i+k} - t_{i+1}}$$

$$N_{i,1}(u) = \begin{cases} 1, & t_i \le \boldsymbol{u} < t_{i+1} \\ 0, & \text{otherwise} \end{cases} \tag{7}$$

Where t_i, called a knot value, exists within the range of u values and adjusts the influence of each control point as shown in Eq. (8):

$$t_i = \begin{cases} 0, & 0 \le i < k \\ i - k + 1, & k \le i \le n \\ n - k + 2, & n < i \le n + k \end{cases} \tag{8}$$

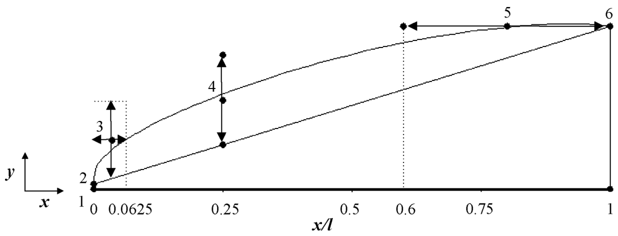

Fig. 7 Nose shape representation using the NURBS curve.

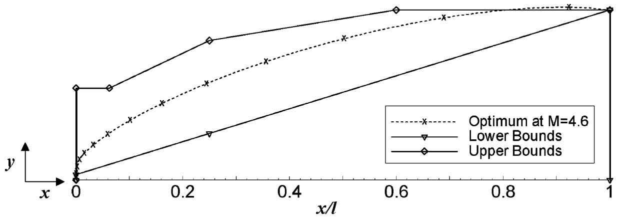

Fig. 8 Selection of design space.

Nose Shape Representation Using the NURBS Curve

The distribution of the control points and the selected design variables to represent the nose shape using the NURBS curve are shown in Fig. 7. For a one-to-one correspondence between the shape function approach and the NURBS curve approach, the number of design variables is set to four.

The number of control points is six. The x coordinate x_1 and y coordinate x_2 of the control point 3, y coordinate x_3 of control point 4, and x coordinate x_4 of the control point 5 are selected as the design variables. By selecting both x and y coordinates as design variables, the control point 3, which is located near the nose tip, can enhance the capability to generate various shapes expected during the shape optimization process, especially near the nose tip, which is important for satisfying the surface heat-transfer constraints. Control point 2 is selected as a fixed point to satisfy the smoothness near the stagnation point and hence is given the same x coordinate as control point 1. The y coordinate of control point 5 is set to the base radius to satisfy the fineness ratio constraint.

Selection of the Design Space

Proper selection of the design space is very important in the optimization process. If the design space is too narrow, a global optimum might not be included in it. If the design space is too wide, then many experimental points are required to build a reliable regression model.

In this study, based on the previously derived single-point optimized shape,[5] a design space wide enough to include the true optimum point is selected.

As shown in Fig. 8, the optimum shape at freestream Mach number of 4.6 is utilized, and the circular cone is the lower bound of the design variables. For design variables 2 and 3, the upper bound is selected relatively wide (optimum shape plus $0.075l$) to include the true optimum point. The selected design space is shown here:

$$0.01l \le x_1 \le 0.0625l, \qquad y_{\text{cone}_1} \le x_2 \le y_{\text{opt}_{M=4.6}} + 0.075l$$

$$y_{\text{cone}_2} \le x_3 \le y_{\text{opt}_{M=4.6}} + 0.075l, \qquad 0.6l \le x_4 \le 1.0l$$

where y_{cone_1} is the y coordinate of the cone at x position and halfway between upper and lower bound of x_1; y_{cone_2} is the y coordinate of the cone at $x/l = 0.25$.

Configuration Design Optimization Using the RSM

The configuration design using RSM consists of the following: 1) design space specification, 2) the experimental point selection, 3) the numerical analyses about the selected points, and 4) the construction of reliable models through regression analysis. The shape optimization process of the multipoint space launcher design is shown in Fig. 9. As shown in the figure, separate response surfaces are

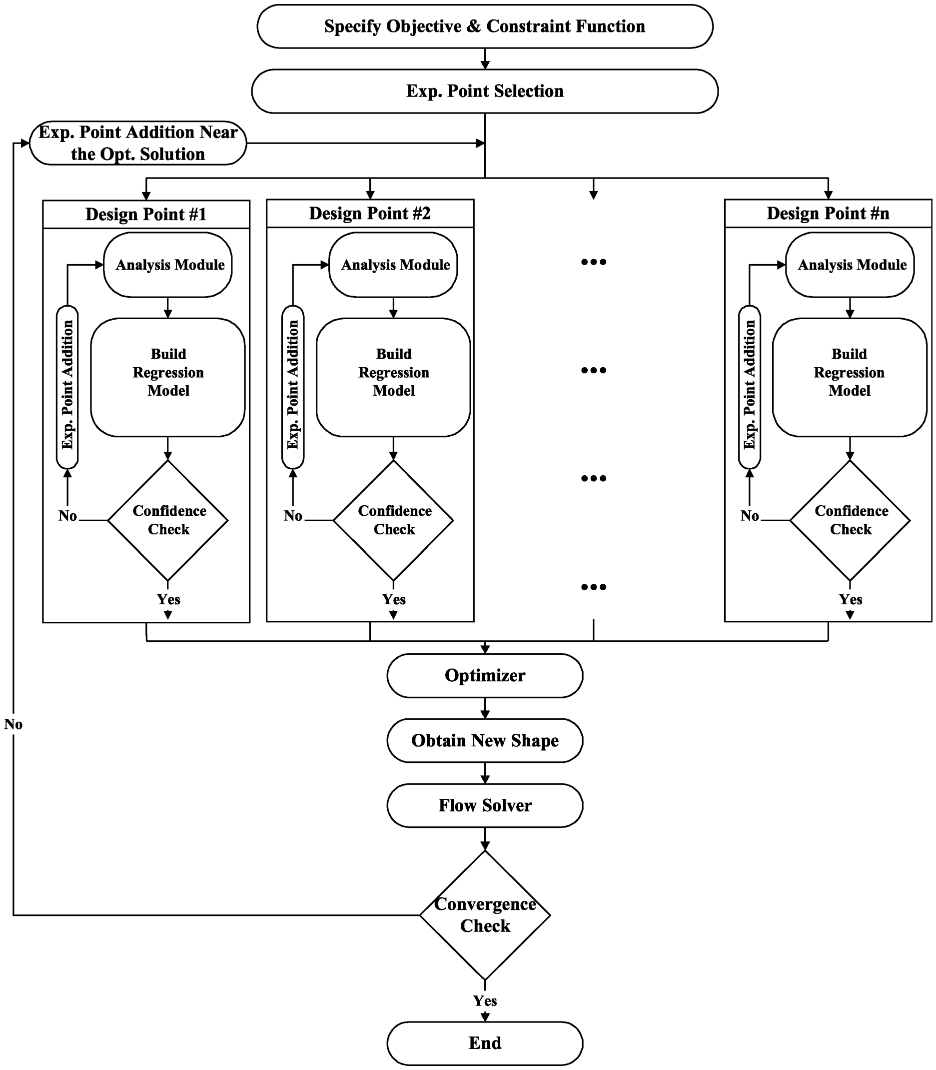

Fig. 9 Multipoint design optimization procedure using the response surface method.

built for each design point (or flight condition) through experiment point selections and analysis calculations. The resultant response surface in each module is combined together using a weighting factor to obtain the optimum shape for the multipoint design problem. A new shape is generated by the optimizer. The new shape is then analyzed by the CFD code, and the predicted objective function by optimizer is compared with the CFD analysis result. If the difference between the predicted value and the CFD analysis result meets the convergence criterion, the final iteration is the new shape.

The objective functions of this study are relatively smooth functions of the design variables, which are caused by the proper selection of the shape functions and control points.

A genetic algorithm, GENOCOP III (Ref. 22), is used for its ability to resolve constrained optimization problems. For the computational grids of 100×85, approximately 10 CPU minutes are required for each axisymmetric Navier–Stokes analysis on a Compaq Alpha Sever DS20E Parallel machine.

Application of the Response Surface Method

It has been demonstrated that RSM with second-order polynomials as design variables can reduce the number of analysis iterations. The design space stretching technique through the design variable transformation can be used to effectively represent the highly nonlinear behavior of the objective function and design constraints.[23]

The response surfaces are built by keeping the maximum radius of nose fairing within the acceptable design range of 90 to 125% of the base radius. The D-optimal design method,[6,24] one of the design of experiment theories, is used to determine the experimental points necessary to build the response surface. A D-optimal design is an n-factor, second-order design, where a minimum number of experimental points is used to minimize the variance by maximizing the determinant of $|X^T X|$, where X is the design matrix. Twenty-three experimental points, which is about 1.5 times the unknown coefficients of the second-order regression model, are finally selected. This is the recommended number of points required to build relatively accurate regression models.[25] Equation (9) represents the generic form of the second-order response surface equation used in this study:

$$R = b_0 + \sum_{i=1}^{k} b_i x_i + \sum_{i=1}^{k} b_{ii} x_i^2 + \sum_{i=1}^{k-1} \sum_{j=i+1}^{k} b_{ij} x_i x_j \tag{9}$$

where R is the response (C_D and C_h in this study), b_0 is the constant coefficient, b_i are the regression coefficients for the first-order terms, b_{ii} are the coefficients for the pure quadratic terms, b_{ij} are the coefficients for the cross-product terms, $x_{i,j}$ are the design variables (shape function parameters or coordinates of control points of NURBS curve), and k is the number of design variables.

The quality of the response surface that has been generated can be estimated by the adjusted R-square, R^2_{adj} (Ref. 6). R^2_{adj} has values between 0 and 1. The value approaches 1 when the response surface generated can be compared closely with the analytical results.

In this study, the response surface of the objective function (drag coefficient) has a value of R^2_{adj} greater than 0.9 without any design space stretching, but for the design constraints (surface heat-transfer rate) the generated response surface has a value of 0.40 when implementing shape functions. To improve the confidence level of the generated response surface, the suboptimization of design space stretching is performed. Hence, the confidence level increases to 0.93 by employing the design space stretching technique. The motivation of the design space stretching is to emphasize and in turn increase the regions of high variation in the natural (unstretched) design space.[23] Detailed explanation about the design space stretching and suboptimization is included in Ref. 23. When implementing the NURBS curve, the regression model for total surface heat-transfer rate has a value greater then 0.9 without implementing design space transformation using stretching.

Design Optimization of Space Launcher Nose Shape

Three critical flight events determined from the performance analysis of the baseline space launcher[26] are listed in Table 1. Design point 1 is a first-stage-burnout condition; design point 2 is the design condition of maximum dynamic pressure; and design point 3 is selected when the drag coefficient reaches its maximum value. The Mach numbers at critical drag and heat-flux values are considered design points because the goal is to minimize drag and surface heat transfer. To calculate the overall drag experienced during the flight, the time history of each flight event is included.

Design Method Validations

In this study, the effectiveness of the optimization method, which implements multiple response surfaces with a weighting factor, is validated. This is done to first minimize drag for the entire flight mission and performed before the multipoint design optimization. The following two design test cases are considered: 1) two-point drag minimization and 2) two-point drag/heat-transfer minimization. Various weighting factors are used to verify the behavior of the design results with each response surface. The nose geometry is modeled by using combined shape functions.

Design Method Validation Case 1

To determine the effect of the weighting factor to the design result, the weighted average of the drag coefficients at design point 1 (first-stage burnout) and design point 2 (maximum dynamic pressure) is selected as the design objective. The stagnation heat transfer at design point 1 and the internal volume of the nose fairing are selected as design constraints. Separate response surfaces are generated for the drag coefficients of design points 1 and 2 and the Stanton number at design point 1. The optimization formulation is as follows:

Minimize

$$F(\boldsymbol{X}) = \omega C_{D1} + (1-\omega)C_{D2}, \qquad 0 \le \omega \le 1$$

Subject to

$$g_1(\boldsymbol{X}) = C_{h1} \le C_{\mathrm{hbaseline}}, \qquad g_2(\boldsymbol{X}) = V \ge V_{\mathrm{baseline}} \tag{10}$$

where

$$C_h = \dot{q}_w / \rho u (h_{\mathrm{aw}} - h_w)$$

In Eq. (10), subscripts 1 and 2 denote the design points.

Because the objective function is dependent on ω, different values of ω generate different optimum shapes (Fig. 10).

Table 1 Performance analysis results of baseline shape[26]

Design point	Event	Mach number	Altitude, km	Time, s
3	Maximum drag coefficient	1.2	5.22	26.7
2	Maximum dynamic pressure	1.8	10.1	38
1	First-stage burnout	4.6	31	62.4

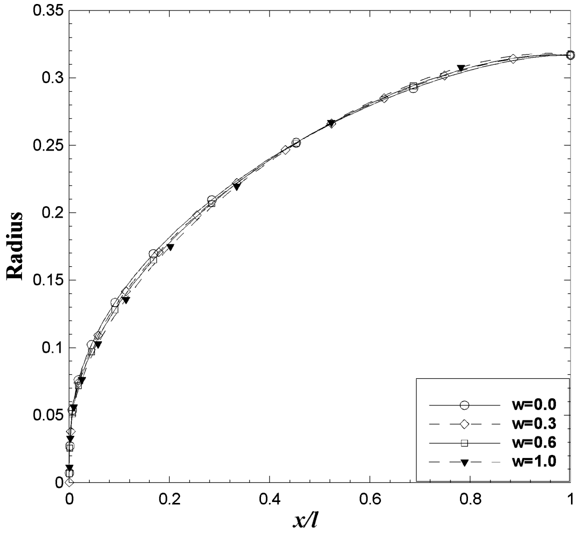

Fig. 10 Optimum shapes with weighting factors.

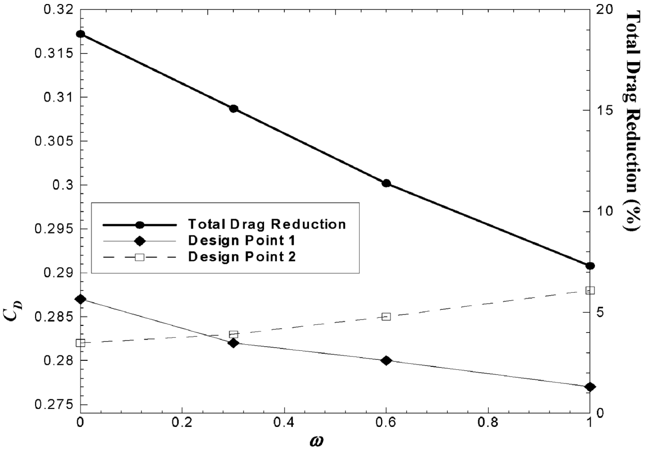

Fig. 11 Drag reduction with weighting factors.

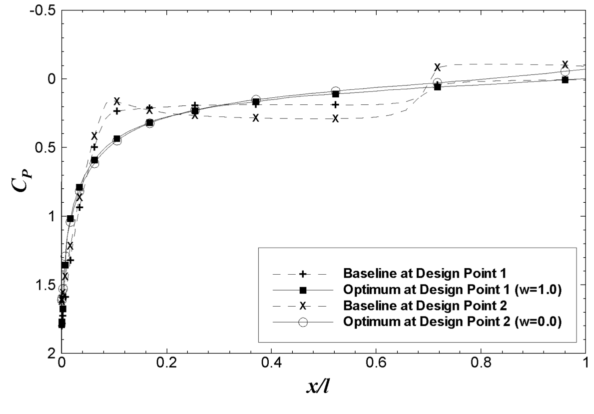

Fig. 12 Comparison of the surface-pressure distributions.

Drag coefficients and percentage reduction in the drag coefficient are compared with the baseline configuration for the different objective functions (or different weighting factor selections) as shown in Fig. 11.

For the case when $\omega = 1$, that is, the configuration optimized to design point 1 has minimum drag at design point 1 as expected and the maximum at design point 2. The reverse is true for the configuration optimized at design point 2 ($\omega = 0$). Considering both design points, the configuration optimized at the design condition of $\omega = 0$ has best drag characteristics. The surface-pressure distributions of the optimized shapes and the baseline configurations are shown in Fig. 12. Optimized shapes have less pressure near the stagnation

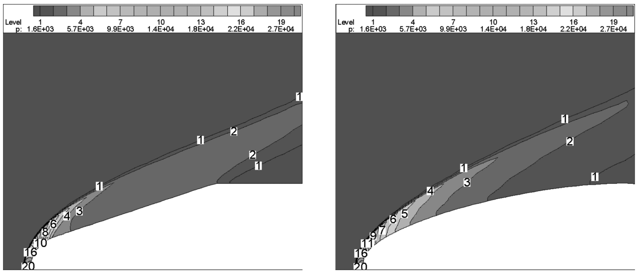

a) Baseline **b) Optimum: $\omega = 1.0$**

(Design point 1)

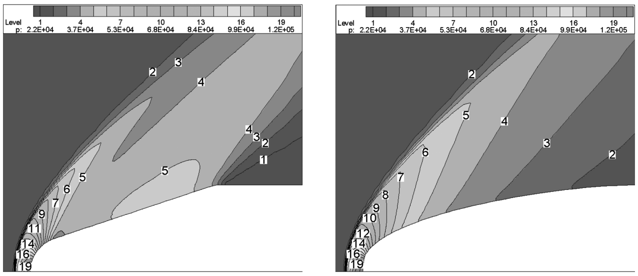

c) Baseline **d) Optimum: $\omega = 0.0$**

(Design point 2)

Fig. 13 Pressure contours of the baseline and optimized nose fairing shapes.

point for both design points, resulting in less drag. The pressure contours of the baseline configurations are compared with the optimized shapes in Fig. 13. A gradual decrease in surface pressure can be observed in the pressure contour plots for the optimized shapes.

Design Method Validation Case 2

The weighted average of drag and surface heat transfer is selected as the design objective because the goal is to minimize both of them. By considering the relative importance of the physical quantities as a function of Mach number and altitude, the surface heat transfer at design point 1 and the drag coefficient at design point 2 are combined to form the design objective for case 2. Furthermore, the impact of the surface heat transfer to the optimized shape will be illustrated through four different weighting factor values from 0 to 1. To keep the aspect ratio constant, an additional constraint is placed on the radius of the configuration. This constraint can prevent aberrant shapes with exceedingly large radius in the nose region. Separate response surfaces are generated for the drag coefficients of design points 2 and the Stanton number at design point 1.

The optimization formulation is as follows:

Minimize

$$F(\boldsymbol{X}) = \omega(C_{D2}/C_{D02}) + (1-\omega)(C_{h1}/C_{h01}), \qquad 0 \le \omega \le 1$$

Subject to

$$g_1(\boldsymbol{X}) = V \ge V_{\text{baseline}}, \qquad g_2(\boldsymbol{X}) = r_{\max} \le r_b \tag{11}$$

where C_{D0} and C_{h0} represent the drag coefficient and Stanton number of the baseline configuration, respectively, and r_b denotes the base radius, and subscripts 1 and 2 denote design points 1 and 2, respectively.

The optimum shapes generated with variable weighting factors are shown in Fig. 14. The nose shape becomes blunt by a decreasing weighting factor, that is, emphasizing the heat transfer at the body surface. The plot of the change of the objective function, drag coefficient at design point 2 and Stanton number at design point 1 as a function of weighting factor, is shown in Fig. 15. As expected, the minimum and maximum Stanton numbers are found to be at $\omega = 0$ (optimum for least surface heat transfer) and $\omega = 1$, respectively. In addition, the drag is large when $\omega = 0$ because then there is no consideration of drag in Eq. (11). However, Fig. 15 shows that the drag is reduced greatly when the objective function includes some fraction of the drag term, that is, ω is greater than zero.

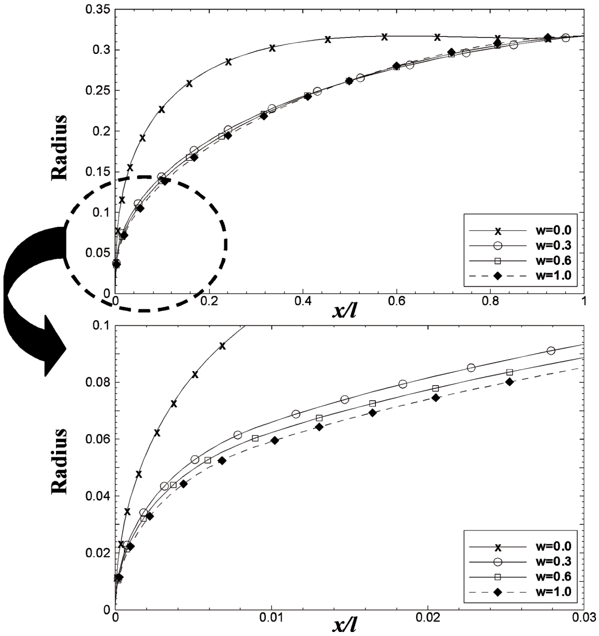

Fig. 14 Comparison of optimum shapes with weighting factors.

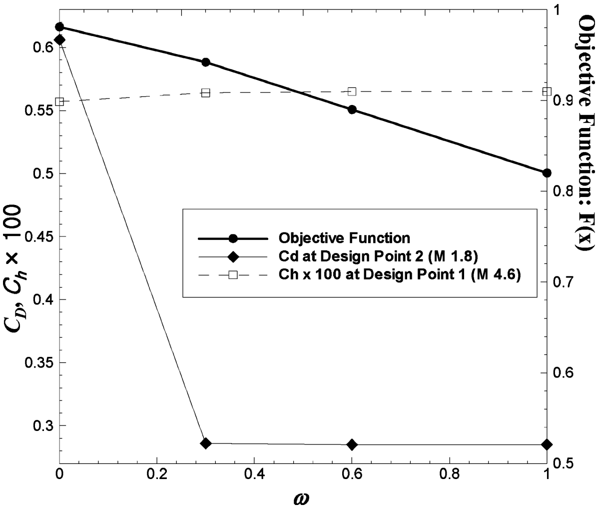

Fig. 15 Objective functions with weighting factors.

From the results of the preceding two design test cases, the optimum designs follow the expected tendency according to the value of the weighting factor. Therefore, the proposed optimization method, which implements separated response surfaces and combines them with a weighting factor, is confirmed.

Three-Points Design Optimization to Minimize Total Drag Experienced During the Flight

For a more practical configuration design, the design objective is to minimized the total drag experienced by the space launcher during the flight from the beginning of the supersonic flight to the first stage burnout. For the whole flight envelope, viscous drag decreases gradually until the drag is negligible at high altitudes. Therefore, the portion of the flight range from Mach 1.0 to first-stage burnout is considered. Heat transfer at design point 1 and the internal volume are selected as constraints. Total drag of the baseline configuration experienced during the flight is plotted as a function of flight time in Fig. 16. Total drag using drag coefficients has been approximated at

Table 2 Comparison of total drag and drag reduction

Shapes designed for	Total drag, N · s	Drag reduction, %
Baseline shape	224,309	0
Design point 1	181,235	19.20
Design point 2	174,731	22.10
Design point 3	177,856	20.71
Multipoint optimum	173,877	22.48

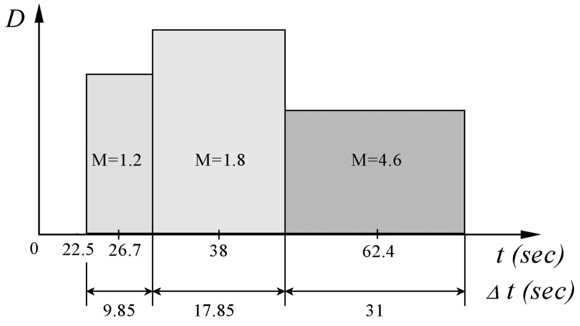

Fig. 16 Flight time and drag of baseline at each design point.

design points 1–3 for computational efficiency. Separate response surfaces are generated for the drag coefficients of design points 1–3 and the Stanton number at design point 1. The multipoint design optimization problem is to find the nose fairing configuration, which has minimum drag during the entire trajectory while satisfying the heat transfer and internal volume constraints. Therefore, an objective function is constructed by combining the drag-coefficient response surface at each design point with dynamic pressure and flight time as weighting factors. Moreover, both the shape function and NURBS curve are introduced to represent body geometry, and the results are compared to propose a proper shape representation technique in this design problem.

Design Optimization Using Shape Functions

The launcher nose's shape is generated using a linear combination of shape functions, as introduced in Eq. (5). The coefficients of the shape functions selected as design variables are the same as those in the preceding two validation cases. The objective function is the integration of drag experienced for the simplified total flight path from Mach 1.0 to first-stage burnout. Therefore, dynamic pressure, flight time, and reference area are multiplied to drag coefficient at each design point and summed to obtain the objective function. The optimization formulation is as follows:

Minimize

$$F(\boldsymbol{X}) = \sum_{i=1}^{3} \omega_i C_{\mathrm{D}i}, \qquad \omega_i = q_i \Delta t_i S_{\mathrm{ref}}, \qquad i = \text{design point}$$

Subject to

$$g_1(\boldsymbol{X}) = C_{h1} \leq C_{\mathrm{h\,baseline}}, \qquad g_2(\boldsymbol{X}) = V \geq V_{\mathrm{baseline}} \tag{12}$$

where Δt is flight time, S_{ref} is the reference area, and V is the total internal volume of the launcher fairing.

The multipoint optimized configuration is compared with the shapes optimized at design points 1, 2, and 3 ($M = 4.6$, $M = 1.8$, $M = 1.2$, respectively) in Fig. 17. As shown in Table 2, the multipoint optimized configuration has the best drag characteristics with approximately a 22.5% reduction in the integrated drag during the supersonic flight mission when compared to the baseline case.

The multipoint optimized shape, which considers the drag experienced for the entire speed range, has similar geometry and drag reduction to the configuration optimized at design point 2 ($M = 1.8$) as shown in Fig. 17. This is because maximum values of dynamic pressure and drag portion are observed at design point 2 on the simplified three-point flight envelope of the launcher (Fig. 18). Design point 1 ($M = 4.6$) has a long flight time but small dynamic pressure, and design point 3 ($M = 1.2$) has a high drag coefficient but short flight time. Optimized shape at design point 1 has the least drag reduction because it has the lowest dynamic pressure in spite of a long flight time. Therefore, if the flight envelope is divided into more design points, it is expected that the multipoint optimized shape considering the whole flight range would have an improved drag performance. In addition, if the heat transfer constraint used is relaxed, then the resulting configuration would be similar to the shape optimized at design point 1 ($M = 4.6$).

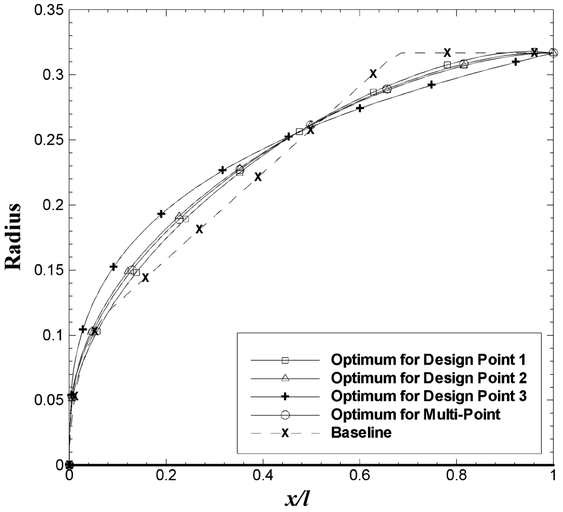

Fig. 17 Comparison of optimum shapes.

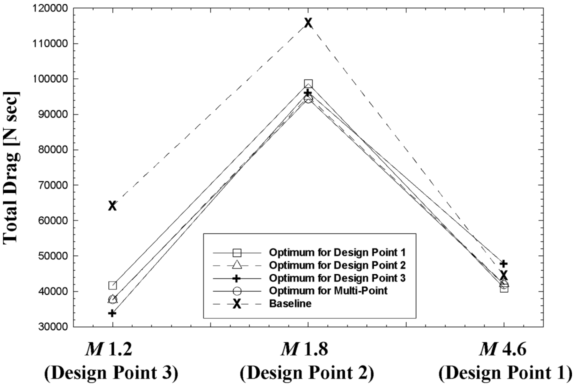

Fig. 18 Total drag comparison.

Design Optimization Using NURBS Curves

The coordinates of the control points for the NURBS curves are selected as the design variables. The design constraints are given by the surface heat-transfer coefficient and the internal volume of the nose fairing.

The mathematical formulation of the design problem is as follows:

Minimize

$$F(\boldsymbol{X}) = \sum_{i=1}^{3} \omega_i C_{\mathrm{D}i}, \qquad \omega_i = q_i \Delta t_i S_{\mathrm{ref}}, \qquad i = \text{design point}$$

Subject to

$$g_1(\boldsymbol{X}) = C_{h1} \leq C_{\mathrm{h\,baseline}}, \qquad g_2(\boldsymbol{X}) = V \geq V_{\mathrm{baseline}} \tag{13}$$

The optimized configuration shapes generated using the shape functions, and the NURBS curves are shown in Fig. 19. The surface-pressure distributions of the generated geometries for each flight condition are shown in Figs. 20–22. In general, the optimized shape using the NURBS curves has lower surface pressures at axial locations around 0.5–50% of the entire body from the nose.

In Table 3, the integrated drag experienced during the flight is compared. From the result it can be shown that 2% performance improvements can be achieved when using the NURBS curve approach than the shape function approach.

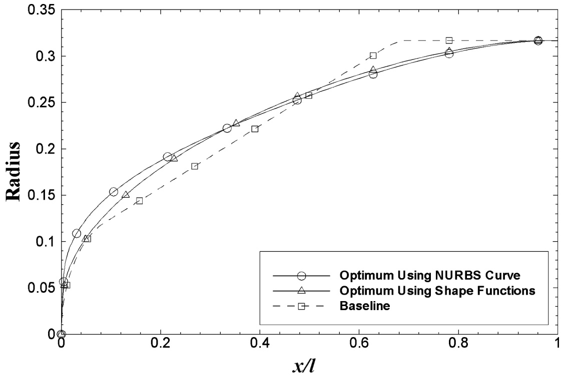

Fig. 19 Comparison of optimum shapes.

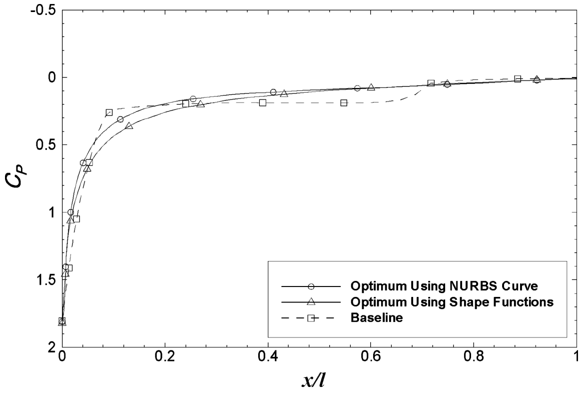

Fig. 20 Comparison of the surface-pressure distributions (design point 1).

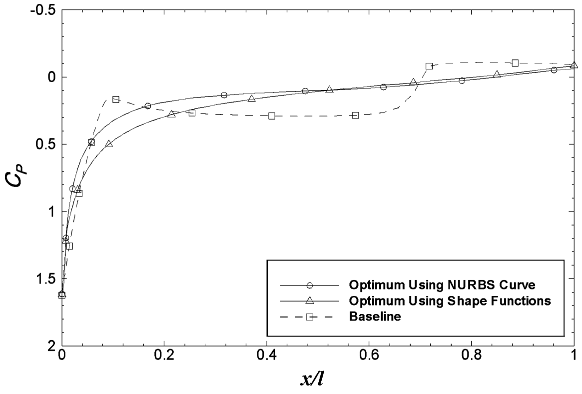

Fig. 21 Comparison of the surface-pressure distributions (design point 2).

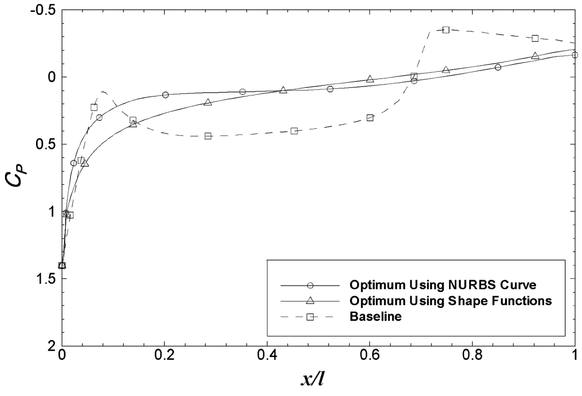

Fig. 22 Comparison of the surface-pressure distributions (design point 3).

Table 3 Comparison of total drag and drag reduction

Shapes	Integrated drag, N · s	Drag reduction, %
Optimum by NURBS	169,686	24.35
Optimum by shape function	173,877	22.48
Baseline shape	224,309	0

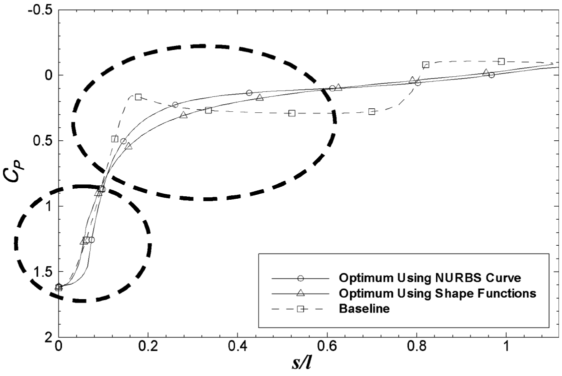

Fig. 23 Surface-pressure distributions along the body surface coordinate (design point 2).

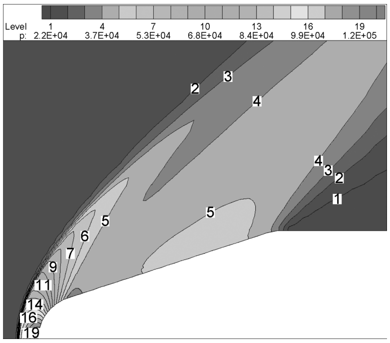

a) Baseline

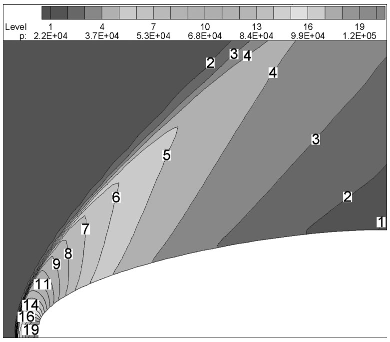

b) Optimum using shape functions

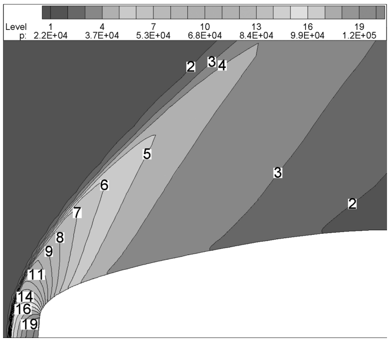

c) Optimum using NURBS curve

Fig. 24 Pressure contours of the baseline and optimized configurations at design point 2.

The surface-pressure distribution as a function of the body surface coordinate s is shown in Fig. 23. As shown in Fig. 19, the optimum shape obtained by using a NURBS geometry representation has a more blunt nose leading to higher surface pressure there. However, the optimum shape obtained by using NURBS has a lower surface pressure as the flow expands at approximately 10–60% of the body surface length from the nose. This causes more drag reduction in NURBS curve approach. With the blunt nose, optimum shape by using NURBS also has better surface heat-transfer characteristics.

The pressure contour plots of the baseline configuration and the optimized configurations obtained with the shape function and with the NURBS curve approaches are shown in Fig. 24 for design point 2. Higher surface pressure near the stagnation point and lower pressure near the flow expansion region can be found in the NURBS curve case.

Conclusions

Single-design-point optimization results in performance degradation for the off-design conditions. Therefore, it is necessary to consider a multipoint optimization formulation. By selecting three design points, that is, the design conditions of maximum drag coefficient, maximum dynamic pressure, and first-stage burnout, multipoint design optimization is performed successfully.

To efficiently reduce the computational time required for numerical optimization, separated response surfaces are generated for each design point and combined together with weighting factors to obtain an objective function. The effectiveness of the design method using separated response surface and weighting factor is validated by showing the tendency of the results for two design test cases, that is, two-points drag minimization and two-points drag/heat-transfer optimization.

It is an important design problem to find the space launcher shape that will have the least amount of integrated drag during the entire flight mission while satisfying heat-transfer constraint. The optimum shape obtained from the aforementioned multipoint design optimization method would experience the minimum integrated drag during the mission. The multipoint derivation involves three flight conditions. Two different geometry generation techniques were implemented, which resulted in successful optimized configurations. These approaches are the shape function approach and the NURBS curve approach with relatively loose heat-transfer constraint. The multipoint optimum configuration has similar geometry and total drag reduction as the shape optimized at design point 2 (M 1.8), but with improved drag performance. This is because design point 2 has the maximum drag. However, if the flight range is divided into more design points, it is expected for the multipoint optimum shape approach would result in further improvements.

By implementing the NURBS curve, a more flexible and versatile representation of the geometry is possible. The result is a better design when using the NURBS-curve-based optimization approach rather than the shape function approach, while keeping the number of control points (four) equal in both approaches. By introducing more control points, a detailed and complex shape can be generated. Therefore, a better design can be expected when using the NURBS curve approach.

For all of the cases considered in this study, the generated response surfaces have good confidence levels using only 23 design points obtained with appropriate stretching of the design space. Using the proposed multipoint design optimization method, a launcher nose shape has been derived that has a greater than 24% improvement in integrated drag performance. The techniques developed in this study can be extended to more general multidiscipline-related design optimization problems.

Acknowledgment

This work was supported by Grant ADD-03-01-01 from the Basic Research Program of the Agency for Defense Development.

References

[1] Lee, J.-W., and Hwang, J. Y., "The Conceptual Design of Air-Launching Micro Space Launcher, Mirinae-1," *Journal of Korean Society for Aeronautical and Space Sciences*, Vol. 29, No. 2, 2001, pp. 117–124.

[2] Hager, J. O., Eyi, S., and Lee, K. D., "Two-Point Transonic Airfoil Design Using Optimization for Improved Off-Design Performance," *Journal of Aircraft*, Vol. 31, No. 5, 1994, pp. 1143–1147.

[3] Kim, H.-J., and Rho, O.-H., "Dual-Point Design of Transonic Airfoils Using the Hybrid Inverse Optimization Method," *Journal of Aircraft*, Vol. 34, No. 5, 1997, pp. 612–618.

[4] Giunta, A. A., Balabanov, V., Haim, D., Grossman, B., Mason, W. H., Watson, L. T., and Haftka, R. T., "Wing Design for a High-Speed Civil Transport Using a Design of Experiments Methodology," AIAA Paper 96-4001, Sept. 1996.

[5] Kim, S.-J., Jeon, K.-S., and Lee, J.-W., "Optimal Design of a Space Launch Vehicle Using Response Surface Method," AIAA Paper 2000-4866, Sept. 2000.

[6] Myers, R. H., and Montgomery, D. C., *Response Surface Methodology*, Wiley, New York, 1995, pp. 279–401.

[7] Burgee, S., Giunta, A. A., Balabanov, V., Grossman, B., Mason, W. H., Narducci, R., Haftka, R. T., and Watson, L., "A Coarse-Grained Parallel Variable-Complexity Multidisciplinary Optimization Paradigm," *International Journal of Supercomputing Applications and High Performance Computing*, Vol. 10, No. 4, 1996, pp. 269–299.

[8] Hirsh, C., "Second-Order Upwind and High-Resolution Schemes," *Numerical Computation of Internal and External, Volume 2: Computational Method for Inviscid and Viscous Flow*, Wiley, New York, 1988, pp. 493–594.

[9] Harten, A., "High Resolution Shemes for Hyperbolic Conservation Laws," *Journal of Computational Physics*, Vol. 49, No. 3, 1983, pp. 357–393.

[10] Yee, H. C., Kolpfer, G. H., and Montague, J. L., "High Resolution Shock Capturing Schemes for Inviscid and Viscous Hypersonic Flows," NASA TM 100097, April 1988.

[11] Yoon, S., and Kwak, D., "Three-Dimensional Incompressible Navier–Stokes Solver Using Lower–Upper Symmetric-Gauss–Seidel Algorithm," *AIAA Journal*, Vol. 29, No. 6, 1991, pp. 874, 875.

[12] Tak, J.-S., "A Study on the Numerical Simulation of the Shock Tunnel," M.S. Thesis, Dept. of Aerospace Engineering, Konkuk Univ., Seoul, Republic of Korea, Dec. 2000.

[13] "Equations, Tables, and Charts for Compressible Flow," NACA R-1135, 1953.

[14] Holden, M. S., and Moselle, J. R., "Theoretical and Experimental Studies of the Shock Wave-Boundary Layer Interaction on Compression Surfaces in Hypersonic Flow," Calspan, Rept. AF-2410-A-1, Oct. 1969; also ARL 70-0002, Jan. 1970.

[15] Rudy, D. H., Thomas, J. L., Kumar, A., Gnoffo, P., and Chakravarthy, S. R., "A Validation Study of Four Navier–Stokes Codes for High-Speed Flows," AIAA Paper 89-1838, June 1989.

[16] Lee, J. Y., and Lewis, M. J., "Numerical Study of the Flow Establishment Time in Hypersonic Shock Tunnels," *Journal of Spacecraft and Rockets*, Vol. 30, No. 2, 1993, pp. 152–163.

[17] Tak, J.-S., Byun, Y.-H., Lee, J.-W., Lee, J.-Y., Huh, C.-J., and Choi, B.-C., "A Numerical Study on the Performance Analysis of Shock Tunnel," *Proceedings of the Korea Society of Computational Fluids Engineering Spring Annual Meeting*, 2000, pp. 39–44.

[18] Vanderplaats, G. N., and Hicks, R. M., "Numerical Airfoil Optimization Using a Reduced Number of Design Coordinates," NASA TM X-73151, 1976.

[19] Lee, J.-W., Lee, Y.-K., Byun, Y.-H., and Hwang, H.-Y., "Design of Space Launch Vehicle Using Numerical Optimization and Inverse Method," *Journal of Spacecraft and Rockets*, Vol. 38, No. 2, 2001, pp. 212–218.

[20] Piegl, L., and Tiller, W., "Curve and Surface Constructions Using Rational B-Splines," *Computer Aided Design*, Vol. 19, No. 9, 1987, pp. 485–498.

[21] Tiller, W., "Rational B-Splines for Curve and Surface Representation," *IEEE Computer Graphics and Application*, Vol. 3, No. 6, 1983, pp. 61–69.

[22] Michalewicz, Z., *Genetic Algorithms + Data Structures = Evolution Programs*, Springer-Verlag, New York, 1996.

[23] Jeon, K.-S., Kim, S.-J., and Lee, J.-W., "Application of Response Surface Method for the Highly Nonlinear Optimization Problems," *Proceedings of the KSAS Spring Annual Meeting*, 2000, pp. 56–59.

[24] Box, M. J., and Draper, N. R., "Factorial Designs, the $|X^T X|$ Criterion, and Some Related Matters," *Technometrics*, Vol. 13, No. 4, 1971, pp. 731–742.

[25] Giunta, A. A., "Aircraft Multidisciplinary Design Optimization Using Design of Experiments Theory and Response Surface Modeling Methods," Ph.D. Dissertation, Dept. of Aerospace and Ocean Engineering, Virginia Polytechnic Inst. and State Univ., Blacksburg, VA, May 1997.

[26] Chae, Y.-S., et al., "Research and Development of KSR-III(I) Final Report," Korea Aerospace Research Inst., Daejeon, Republic of Korea, Aug. 1998.

J. Korte
Associate Editor